Controlling contaminants using a far-UVC-based advanced oxidation process for potable reuse

Ran Yin [1,2], Claire E. Anderson [2], Jing Zhao [1], Alexandria B. Boehm [2] & William A. Mitch [2][envelope]

Increasing the efficiency of the processing units used to purify municipal wastewater to potable quality would enhance the sustainability of potable reuse. Conventional advanced oxidation processes using 254 nm UV light degrade contaminants by both direct photolysis and reaction with radicals produced by hydrogen peroxide photolysis. Treatment goals include 0.5-log removal of 1,4-dioxane, reducing N-nitrosodimethylamine to <10 ng l^{-1} and 6-log virus inactivation. Using three potable reuse waters, we demonstrate here that a switch from 254 to 222 nm (far-UVC) achieved all three treatment goals at ~320 mJ cm^{-2} UV fluence, which is around fourfold less than is needed at 254 nm. Developing and validating a kinetic model, we determined that the increased energy efficiency arises from a 2.1- to 7.5-fold increase in direct photolysis and a 3.6-fold increase in radical concentrations. Compared with switching to far-UVC wavelengths, alternative efforts to switch from H$_2$O$_2$ to chlorine have been frustrated by the need to increase UV fluence to control N-nitrosodimethylamine.

Utilities are increasingly considering purifying municipal wastewater (potable reuse) to supplement conventional water supplies stressed by population growth and climate change[1–3]. Potable reuse provides a reliable, local water supply that is ~40% less costly and ~60% less energy-intensive than seawater desalination[4]. Potable reuse treatment trains in coastal regions (for example, Australia, Singapore and California[5–7]) employ full advanced treatment processes, combining microfiltration, reverse osmosis (RO) and an advanced oxidation process (AOP), to remove microbial and chemical contaminants[4,8,9]. Research has focused on optimizing RO treatment as this accounts for ~50% of the 1–2.5 kWh m^{-3} energy intensity of full advanced treatment trains[4,10]. A greater focus on improving the efficiency of other treatment train components would enhance the sustainability of potable reuse as a water supply alternative.

The AOP presents a promising prospect for further optimization. AOPs serve as a final barrier to remove pathogens[11] and contaminants that pass through RO membranes, particularly low-molecular-weight, neutral compounds such as the potent carcinogen N-nitrosodimethylamine (NDMA) and the industrial solvent 1,4-dioxane[9]. Conventional systems use 254 nm UV light emitted by low-pressure mercury lamps in the presence of hydrogen peroxide (the UV/H$_2$O$_2$ AOP). Pathogens and certain chemical contaminants (for example, NDMA) can be degraded by direct UV photolysis. The photolysis of H$_2$O$_2$ by a photon of 254 nm light ($h\nu$) generates hydroxyl radicals (HO·; equation (1)), which can oxidize chemicals that do not absorb UV light (for example, 1,4-dioxane). Treatment metrics to validate AOPs include (1) 6-log inactivation of viruses, often demonstrated by spiking tests using non-pathogenic MS2 bacteriophage as a surrogate, (2) the degradation of NDMA to <10 ng l^{-1} and (3) 0.5-log removal of 1,4-dioxane[9]. Because of the inefficiency of the UV/H$_2$O$_2$ AOP, reaching these targets requires a very high UV fluence (~800–1,000 mJ cm^{-2})[9]. Even so, because H$_2$O$_2$ absorbs poorly at 254 nm (molar absorption coefficient at 254 nm, $\varepsilon_{254} = 18.6$ M^{-1} cm^{-1})[12], only ~10% is photolysed to produce HO· (ref. 9).

$$H_2O_2 + h\nu \rightarrow 2HO\cdot \tag{1}$$

[1]Department of Civil and Environmental Engineering, The Hong Kong University of Science and Technology, Hong Kong, China. [2]Department of Civil and Environmental Engineering, Stanford University, Stanford, CA, US. [envelope]e-mail: wamitch@stanford.edu

Recent attempts to switch from H_2O_2 to chlorine (HOCl) as a more efficient radical source (equation (2)) have met with limited success. Radical production and 1,4-dioxane degradation are more efficient, because HOCl has a higher UV absorbance at 254 nm ($\varepsilon_{254} = 62$ M^{-1} cm^{-1}) as well as a higher quantum yield (0.62 versus 0.50)[13]. Although exposure to chlorine also inactivates pathogens, research has indicated that the UV/HOCl AOP may lead to the formation of NDMA via reactions between HOCl and inorganic chloramines in the RO permeate originating from chloramines applied upstream to control membrane biofouling[14]. Thus, although a lower UV fluence is needed to control pathogens and 1,4-dioxane, utilities may need to increase UV fluence to control the additional NDMA[13–15].

$$HOCl + h\nu \rightarrow HO\cdot + Cl\cdot \tag{2}$$
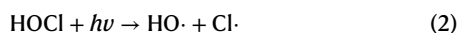
An alternative is to use lower wavelengths (far-UVC), where HO· production from H_2O_2 is more efficient. The krypton chloride (KrCl) excimer lamp, which emits mainly at 222 nm, has recently been developed as a novel UV radiation source for disinfection[16–18]. Compared with conventional mercury lamps, this excimer lamp avoids the risk of mercury leakage into treated waters during lamp breakage and is much less damaging to human skin and eye tissue[16,19]. Bench-scale studies in deionized water revealed that the inactivation rate constants of coronavirus, poliovirus and rotavirus are two to ten times higher at 222 nm than at 254 nm (refs. [20–22]). A recent study of the UV/H_2O_2 AOP indicated that steady-state concentrations of HO· are 9.4-fold greater in deionized water and 3.7-fold greater in groundwater at 222 nm than at 254 nm (ref. [23]). A portion of the enhancement is due to the greater absorbance of H_2O_2 at 222 nm (97.7 M^{-1} cm^{-1} versus 18.6 M^{-1} cm^{-1}), although the quantum yield for H_2O_2 at 222 nm is unknown. The lower enhancement in groundwater relative to deionized water reflects the strong competition for UV absorbance at 222 nm as well as HO· scavenging by groundwater matrix components. However, the UV/H_2O_2 AOP using 222 nm light (the UV$_{222}$-based AOP) has not been applied to RO permeate in wastewater reuse contexts, and critical information needed to model process performance in this matrix (for example, the quantum yields of H_2O_2 and important matrix components) is lacking.

Using a synthetic RO permeate, in this study we developed and validated a kinetic model to predict the performance of the UV$_{222}$-based AOP in RO permeate. Quantum yields were measured for H_2O_2 and the inorganic monochloramine (NH$_2$Cl) and dichloramine (NHCl$_2$) that occur in RO permeate; chloramines are important competitors with H_2O_2 for the absorption of UV light and are the predominant scavengers of HO·, but they also produce the reactive radical Cl·, which can contribute to contaminant degradation (equations (3) and (4))[12]. Using three authentic RO permeates from potable reuse facilities, we determined that the UV$_{222}$-based AOP could achieve 6-log inactivation of MS2 bacteriophage, control NDMA at <10 ng l^{-1} and attain 0.5-log removal of 1,4-dioxane at around fourfold lower UV fluence than is needed at 254 nm. Beyond these typical treatment objectives, we also observed the degradation of regulated (for example, trihalomethanes) and unregulated (for example, haloacetonitriles) halogenated disinfection by-products (DBPs) at two- to threefold lower UV fluence. Halogenated DBPs occur in RO permeate at concentrations closer to levels of health concern than pharmaceuticals and many other contaminant classes[9]. After forming from chloramine reactions upstream of RO, many low-molecular-weight, neutral halogenated DBPs pass through RO membranes and are poorly removed by the UV/H_2O_2 AOP at 254 nm (refs. [13,15,24]). Our results demonstrate that switching to the UV$_{222}$-based AOP could substantially increase the efficiency of AOP treatment, further enhancing potable reuse as a sustainable water supply alternative.

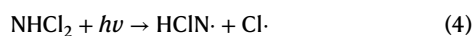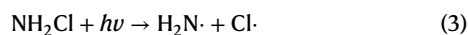$$NH_2Cl + h\nu \rightarrow H_2N\cdot + Cl\cdot \tag{3}$$

$$NHCl_2 + h\nu \rightarrow HClN\cdot + Cl\cdot \tag{4}$$

Table 1 | Parameters for direct UV photolysis at 222 and 254 nm

Contaminant	k_{222}/k_{254}	ε_{222} (M^{-1}cm^{-1})	Φ_{222}	ε_{254} (M^{-1}cm^{-1})	Φ_{254}
Trichloromethane	5.45	33.5	0.38	7.9	0.26
Bromodichloromethane	3.63	81.4	0.61	33.7	0.48
Dibromochloromethane	2.86	332.5	0.72	136.5	0.53
Tribromomethane	3.93	1,686.7	0.55	489.8	0.42
Dichloroacetonitrile	7.19	16.8	0.57	3.1	0.38
Bromochloroacetonitrile	7.51	850.4	0.35	171	0.20
Dibromoacetonitrile	2.42	886.9	0.45	386.7	0.37
N-Nitrosodimethylamine	6.49	29,434.2	0.44	6,372.3	0.27
N-Nitrosomorpholine	2.11	8,583.3	0.43	6,013.2	0.25
1,4-Dioxane	5.45	38.4	0.34	9.4	0.22
Oxidant	$\Phi_{222}\varepsilon_{222}/\Phi_{254}\varepsilon_{254}$	ε_{222} (M^{-1}cm^{-1})	Φ_{222}	ε_{254} (M^{-1}cm^{-1})	Φ_{254}
H_2O_2	4.5	97.7	0.43	18.6	0.50
NH$_2$Cl	0.8	188	0.55	371	0.35
NHCl$_2$	8.2	1,105.8	0.76	136	0.75

Direct photolysis by the UV$_{222}$- and UV$_{254}$-based AOPs

Kinetic models enable the prediction of contaminant degradation under different conditions, while highlighting fundamental factors responsible for differences in the efficiency between two systems. In the UV/H_2O_2 AOP, contaminants are degraded via (1) direct UV photolysis and (2) oxidation by HO· generated from H_2O_2 photolysis. Under conditions of low UV absorbance (for example, deionized water), the direct UV photolysis of contaminants can be described by equation (5), where C is the concentration of a contaminant at time t, I_0 is the incident fluence rate (mW cm^{-2}), Φ is the unitless quantum yield, ε is the molar absorption coefficient (M^{-1} cm^{-1}) and U is the energy associated with an einstein of photons (J einstein^{-1}) of 222 or 254 nm UV light[25]. Four chlorinated and brominated trihalomethanes, three chlorinated and brominated dihaloacetonitriles, two *N*-nitrosamines (NDMA and *N*-nitrosomorpholine (NMOR)) and 1,4-dioxane were treated separately in deionized water with 222 or 254 nm UV light. Plots of ln (C/C_0) versus time, where C_0 is the initial contaminant concentration, demonstrated that the direct UV photolysis of each compound (1 µM) fit first-order kinetics (Extended Data Figs. 1 and 2), as expected based on equation (5). The UV fluence-based degradation rate constants (Supplementary Table 1) were calculated to be 2.1- to 7.5-fold higher at 222 nm than at 254 nm (Table 1).

$$-\frac{dC}{dt} = \frac{2.303 I_0 \Phi \varepsilon}{U} \times C \tag{5}$$

The two parameters defining contaminant susceptibility to direct photolysis are ε and Φ (equation (5)). The ε values measured in deionized water for these compounds (full spectra are provided in Extended Data Fig. 3) were 1.4- to 4.8-fold higher at 222 nm than at 254 nm. Table 1 also provides the Φ values determined by fitting compound decay (Extended Data Figs. 1 and 2) to equation (5) using the ε values and the incident fluence rate (determined by iodide–iodate actinometry[26,27]); the Φ values at 254 nm generally agreed with literature values (Supplementary Table 2). The Φ values were higher at 222 nm than at 254 nm for each compound, reflecting the greater tendency for photodegradation after absorption of the higher-energy 222 nm photons. The compounds showing the smallest increases in the fluence-based direct photolysis rate constants (dibromoacetonitrile and NMOR) when switching from 254 to 222 nm exhibited the smallest increases in ε values (Table 1).

Table 2 | Model-simulated steady-state radical concentrations under different conditions

	222nm			254nm		
	HO· (M)	Cl· (M)	Cl$_2^-$ (M)	HO· (M)	Cl· (M)	Cl$_2^-$ (M)
UV/H$_2$O$_2$[a]	5.86×10^{-12}	NA	NA	1.58×10^{-12}	NA	NA
UV/H$_2$O$_2$/chloramines[b]	1.82×10^{-12}	2.21×10^{-15}	6.14×10^{-14}	5.08×10^{-13}	2.40×10^{-15}	6.79×10^{-14}
UV/chloramines[c]	3.89×10^{-13}	3.20×10^{-15}	8.99×10^{-14}	3.57×10^{-13}	2.83×10^{-15}	8.00×10^{-14}

[a][H$_2$O$_2$]$_0$=3.4 mg l^{-1}, [HCO$_3^-$]$_0$=50 mg l^{-1}, pH 5.6 and UV fluence rate=1.1 mW cm^{-2}. [b][H$_2$O$_2$]$_0$=3.4 mg l^{-1}, [NH$_2$Cl]$_0$=3.5 mg$_{Cl_2}$ l^{-1}, [NHCl$_2$]$_0$=1.5 mg$_{Cl_2}$ l^{-1}, [HCO$_3^-$]$_0$=50 mg l^{-1}, pH 5.6 and UV fluence rate=1.1 mW cm^{-2}. [c][NH$_2$Cl]$_0$=3.5 mg$_{Cl_2}$ l^{-1}, [NHCl$_2$]$_0$=1.5 mg$_{Cl_2}$ l^{-1}, [HCO$_3^-$]$_0$=50 mg l^{-1}, pH 5.6 and UV fluence rate=1.1 mW cm^{-2}. NA, not applicable.

Radical concentrations in the UV$_{222}$- and UV$_{254}$-based AOPs

AOP treatment produces HO· by photolysis of the ~3.4 mg l^{-1} (~100 μM) H$_2$O$_2$ typically added to RO permeate, and Cl· by photolysis of the ~1.1 mg Cl$_2$ per litre (hereafter mg$_{Cl_2}$ l^{-1}; ~16 μM) NH$_2$Cl (equation (3)) and ~1.1 mg$_{Cl_2}$ l^{-1} (~7.5 μM) NHCl$_2$ (equation (4)) occurring in RO permeate (Supplementary Table 3). While the molar absorption coefficients at 222 nm are higher than those at 254 nm by around fivefold for H$_2$O$_2$ and around eight-fold for NHCl$_2$, the molar absorption coefficient for NH$_2$Cl is two-fold lower (Table 1).

Determining the Φ values for the direct photolysis of H$_2$O$_2$ and chloramines requires a more complicated procedure than that used for the compounds discussed above because the radicals produced by direct photolysis react with H$_2$O$_2$ and chloramines, such that their decay rate constants result from both direct photolysis and their reactions with these radicals (equation (6), where k_{obs} is the experimentally determined rate constant and R is a radical that reacts with H$_2$O$_2$ or chloramines with rate constant k_R). Instead, an existing kinetic model containing 119 elementary reactions (Supplementary Table 4) involving radicals was used to model the radical reactions, encompassing the second term in equation (6); the accuracy of this kinetic model has been validated in UV$_{254}$/H$_2$O$_2$ AOP pilot studies involving the treatment of authentic RO permeates containing chloramines[12]. For UV treatment at 222 nm, the primary unknown is the direct photolysis quantum yield (Φ in equation (6)). For the treatment of H$_2$O$_2$, NH$_2$Cl or NHCl$_2$ in deionized water at 222 nm, their experimentally observed degradation was compared with model results using various Φ values (Extended Data Fig. 4), with the optimal Φ values determined by least-squares fitting (Table 1). Driven by both photon absorption and quantum yield (that is, $\Phi\varepsilon$ in equation (5)), radical production from H$_2$O$_2$ was 4.5-fold higher at 222 nm than at 254 nm, and 8.2-fold higher from NHCl$_2$. For NH$_2$Cl, although the ε value was two-fold lower at 222 nm, radical production was only ~20% lower (as indicated by $\Phi\varepsilon$) because of the substantially higher Φ value at 222 nm compared with at 254 nm (Table 1). These findings are important because NH$_2$Cl is considered the major competitor for photon absorption in conventional UV$_{254}$/H$_2$O$_2$ AOP systems due to its strong UV absorbance (ε)[12,15]. Hydroxyl radical production by H$_2$O$_2$ photolysis should be enhanced by the reduced competition for photons resulting from the lower absorbance by NH$_2$Cl at 222 nm, and when NH$_2$Cl does absorb 222 nm photons, its higher Φ value at 222 nm would promote the production of Cl· radicals, contributing to contaminant degradation.

$$k_{obs} = \frac{2.303 I_0 \Phi \varepsilon}{U} + k_R[R] \qquad (6)$$

The ε and Φ values were used in the kinetic model to predict the steady-state concentrations of HO·, Cl· and Cl$_2^-$ radicals generated in three scenarios during irradiation at 222 or 254 nm under conditions relevant to AOP treatment of RO permeate (pH 5.6, 50 mg l^{-1} HCO$_3^-$ and 1.1 mW cm^{-2} incident fluence rate): (1) 100 μM (3.4 mg l^{-1}) H$_2$O$_2$ alone, (2) 50 μM (3.5 mg$_{Cl_2}$ l^{-1}) NH$_2$Cl and 11 μM (1.5 mg$_{Cl_2}$ l^{-1}) NHCl$_2$, and (3) a mixture of 100 μM H$_2$O$_2$, 50 μM NH$_2$Cl and 11 μM NHCl$_2$. In experiments

conducted under the same conditions, nitrobenzene (which reacts only with HO·)[28] and benzoic acid (which reacts with HO· and Cl·)[29] were used as probes to measure the steady-state concentrations of HO· and Cl·. The steady-state concentrations of HO· and Cl· calculated by the kinetic model (Table 2) agreed with those measured experimentally via the probes (Supplementary Table 5) within 12% on average (7% standard deviation; $n = 10$), indicating the accuracy of the kinetic model.

During treatment of H$_2$O$_2$ alone, the HO· concentration was 3.7-fold higher under 222 nm irradiation than under 254 nm irradiation (Supplementary Table 6), reflecting the substantial enhancement of H$_2$O$_2$ direct photolysis ($\Phi\varepsilon$ in equation (6) and Table 1). During UV treatment of the mixture of H$_2$O$_2$ and chloramines at 222 nm, the HO· concentration was 3.2-fold lower than without chloramines, reflecting both substantial competition by chloramines for photon absorption and the strong scavenging of HO· by chloramines ($k = 1.02 \times 10^9$ M^{-1} s^{-1} for NH$_2$Cl and $k = 6.21 \times 10^8$ M^{-1} s^{-1} for NHCl$_2$)[15]. However, the HO· concentration was still 3.6-fold higher during irradiation at 222 nm than at 254 nm, while the concentrations of Cl· and Cl$_2^-$ were ~10% lower (Supplementary Table 6). During irradiation of chloramines alone, the concentrations of HO·, Cl· and Cl$_2^-$ radicals were ~10% higher under 222 nm irradiation than under 254 nm irradiation, reflecting a balance between the decrease in photolysis of NH$_2$Cl, the dominant chloramine species, and the increase in NHCl$_2$ photolysis (Table 1). In addition to the 2.1- to 7.5-fold increase in the direct photolysis of target contaminants (Table 1), both the model and experimental results indicate that switching from 254 to 222 nm should result in an ~3.6-fold increase in contaminant degradation by HO· during treatment of typical mixtures of H$_2$O$_2$ and chloramines encountered during AOP treatment of RO permeate.

Contaminant degradation by the UV$_{222}$- and UV$_{254}$-based AOPs

The degradation of 1 μM 1,4-dioxane in three authentic RO permeates containing 100 μM (3.4 mg l^{-1}) H$_2$O$_2$ and chloramine concentrations in the range of 1.6–2.8 mg$_{Cl_2}$ l^{-1} (Supplementary Table 3) followed first-order kinetics during irradiation with either 222 or 254 nm UV light (Extended Data Fig. 5). The incident fluence-based degradation rate constants measured within the UV$_{222}$-based AOP were 4.0-, 3.4- and 4.8-fold higher in the RO permeate samples from facilities 1, 2 and 3, respectively, than those measured in the UV$_{254}$-based AOP ($P = 3.8 \times 10^{-7}$; Fig. 1a). As a result, the UV fluences needed to achieve the 0.5-log removal target for potable reuse facilities were 282, 305 and 375 mJ cm^{-2} at 222 nm for the RO permeate samples from facilities 1, 2 and 3, respectively. These fluences were 3.4- to 4.8-fold lower than the 1,140, 1,047 and 1,786 mJ cm^{-2} needed at 254 nm for facilities 1, 2 and 3, respectively. The fluence values at 254 nm are comparable to the values reported previously under similar conditions[30]. The experimental fluence-based degradation rate constant of 1,4-dioxane in a synthetic RO permeate containing 3.4 mg l^{-1} H$_2$O$_2$, 3.5 mg$_{Cl_2}$ l^{-1} NH$_2$Cl and 1.5 mg$_{Cl_2}$ l^{-1} NHCl$_2$ was also 3.7-fold higher for the UV$_{222}$-based AOP than for the UV$_{254}$-based AOP, concurring with the results of the kinetic model (Extended Data Fig. 6). The fluence-based degradation rate constants for 1,4-dioxane were fairly well predicted by the kinetic model for the RO permeates from facilities 1 and 2, but less so for the permeate from facility 3.
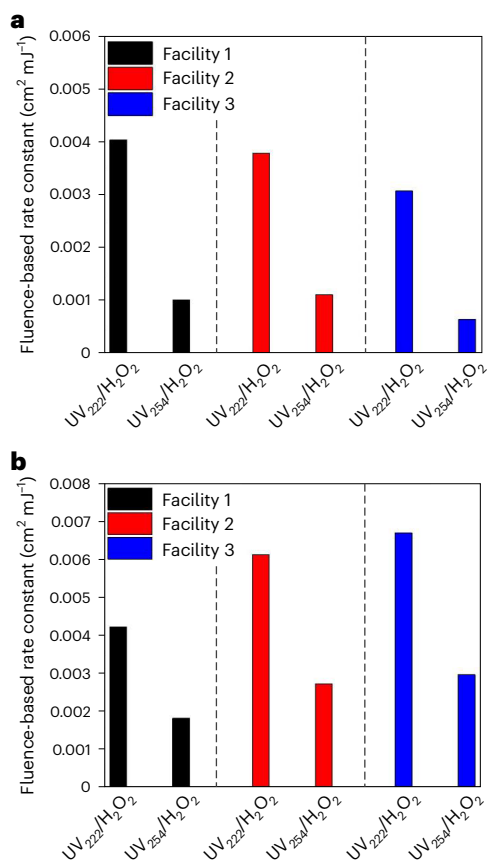
Fig. 1 | Comparison of degradation rate constants for 1,4-dioxane and NDMA using the UV$_{222}$- and UV$_{254}$-based AOPs. a,b, Incident fluence-based degradation rate constants for 1 μg l^{-1} 1,4-dioxane (**a**) and 50 ng l^{-1} NDMA (**b**) using the UV$_{222}$- and UV$_{254}$-based AOPs in authentic RO permeates from facilities 1–3 spiked with 100 μM (3.4 mg l^{-1}) H$_2$O$_2$.

Fig. 2 | Comparison of halogenated DBP degradation rate constants using the UV$_{222}$- and UV$_{254}$-based AOPs. Incident fluence-based degradation rate constants for 100 μg l^{-1} TCM, BDCM and DCAN spiked into authentic RO permeates collected from facilities 1–3 using the UV$_{222}$- and UV$_{254}$-based AOPs.

UV$_{254}$-based AOPs were substantial for TCM (~3.1-fold; $P = 1.1 \times 10^{-6}$), BDCM (~7.7-fold; $P = 2.0 \times 10^{-7}$) and DCAN (~2.7-fold; $P = 1.1 \times 10^{-4}$).

Virus inactivation by the UV$_{222}$- and UV$_{254}$-based AOPs

For each UV-based AOP, the slopes of the logarithmic plots of the inactivation of MS2 bacteriophage spiked into RO permeate samples versus UV fluence were not significantly different ($P = 0.76$ and 0.11 for the UV$_{222}$- and UV$_{254}$-based AOPs, respectively) across the three RO permeate samples (Fig. 3). However, the incident fluence-based inactivation rate constant for the UV$_{222}$-based AOP (4.61×10^{-2} cm^2 mJ^{-1}) was 35% higher than that for the UV$_{254}$-based AOP (3.43×10^{-2} cm^2 mJ^{-1}; $P = 0.035$). Therefore, 6-log inactivation of MS2 bacteriophage, a typical target for AOP treatment in potable reuse facilities, would require 130 mJ cm^{-2} using the UV$_{222}$-based AOP, but 175 mJ cm^{-2} for the UV$_{254}$-based AOP.

Discussion

While potable reuse represents a reliable and less costly and energy-intensive alternative to seawater desalination[4] for expanding water supplies in drought-prone areas, further improvements in the efficiency of potable reuse treatment trains are needed. Effort has deservedly been focused on optimizing the RO process, which accounts for ~50% of the energy consumption of RO-based reuse trains[4]. Increasing the efficiency of AOP treatment would also contribute to the sustainability of potable reuse, but the modified AOP must still achieve three key treatment goals. First, AOPs target 0.5-log removal of 1,4-dioxane, an indicator of AOP performance with respect to radical-mediated degradation of the low-molecular-weight, neutral compounds that pass through RO membranes[9]. In addition to 1,4-dioxane, such compounds include industrial solvents and DBPs, while higher-molecular-weight contaminants are well rejected by RO[9]. Second, AOPs aim to degrade *N*-nitrosamines by direct photolysis to <10 ng l^{-1}. Of the two *N*-nitrosamines most commonly detected in potable reuse trains, NDMA typically is of greater concern because NMOR is well rejected by RO membranes[15]. Lastly, potable reuse trains in California seek to accumulate 12-log inactivation of viruses across the potable reuse train, with 6-log inactivation a typical goal for the AOP process[9].

For treatment of RO permeates, the UV$_{254}$/H$_2$O$_2$ AOP has been favoured over the ozone/H$_2$O$_2$ AOP because it features substantially lower capital costs for smaller facilities (~0.5 m^3 s^{-1})[33], and also because the ozone/H$_2$O$_2$ AOP does not effectively degrade NDMA[13]. Recent efforts to improve the AOP process have focused on switching oxidants from H$_2$O$_2$ to chlorine as the source of radicals on irradiation at 254 nm (refs. 13–15,34). Compared with H$_2$O$_2$, chlorine features greater UV absorbance ($\varepsilon_{254} = 62$ M^{-1} cm^{-1} versus 18.6 M^{-1} cm^{-1}) and

Research is needed to constrain the reactivity of dissolved organic matter to further optimize the kinetic model (Extended Data Fig. 7).

The degradation of 50 ng l^{-1} NDMA also followed first-order kinetics (Extended Data Fig. 8). The incident fluence-based degradation rate constants determined for the UV$_{222}$-based AOP were 2.3-fold higher than those using the UV$_{254}$-based AOP for samples from all three facilities ($P = 4.5 \times 10^{-4}$) (Fig. 1b). The 383, 264 and 241 mJ cm^{-2} UV fluences needed to reduce NDMA concentrations to California's 10 ng l^{-1} Notification Limit[13] using 222 nm UV light were ~2.3-fold lower than the 890, 594 and 546 mJ cm^{-2} fluences needed at 254 nm for samples from facilities 1, 2 and 3, respectively.

Probably formed via reactions with chloramines applied upstream to control membrane biofouling, trichloromethane (TCM), bromodichloromethane (BDCM) and dichloroacetonitrile (DCAN) were detected at concentrations in the range of 2.03–5.14, 1.21–3.66 and 0.19–0.57 μg l^{-1}, respectively, in the RO permeate samples collected from facilities 1, 2 and 3. Their detection in the RO permeates highlights their potential to pass through RO membranes. While TCM and BCDM are two of the four trihalomethanes regulated in drinking water[31], DCAN contributes more to the cytotoxicity of disinfected drinking waters, despite occurring at lower concentrations, due to its high cytotoxic potency[31,32]. When 100 μg l^{-1} TCM, BDCM or DCAN was spiked into the three RO permeate samples, the fluence-based degradation rate constants were highest for BDCM for both the UV$_{222}$- and UV$_{254}$-based AOPs (Fig. 2). Brominated DBPs feature stronger UV absorbance (Table 1) and greater reactivity with HO· (ref. 30). The increases in fluence-based degradation rate constants when switching between the UV$_{222}$- and
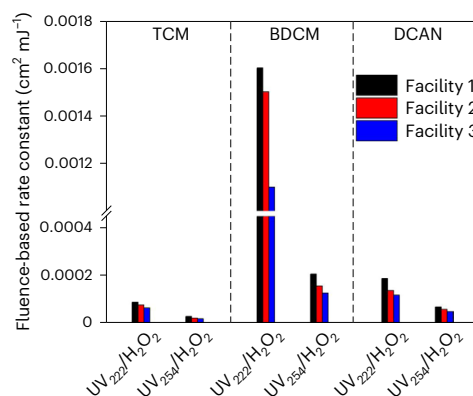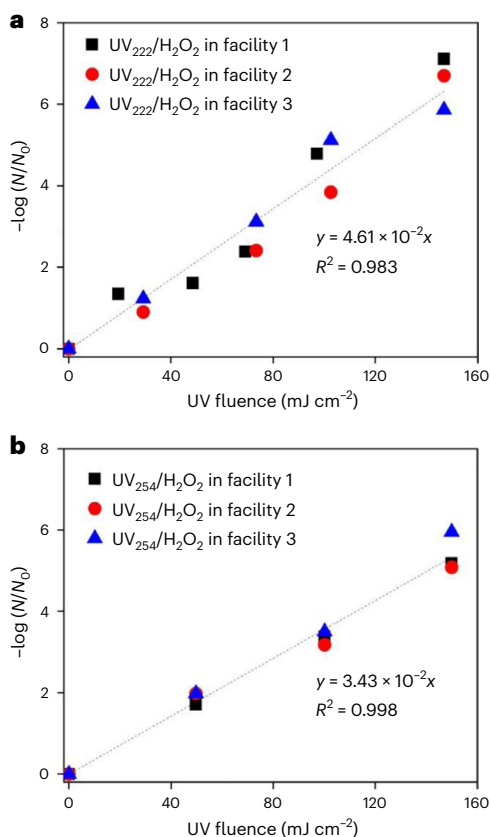
Fig. 3 | Comparison of the inactivation rates of MS2 bacteriophage for the UV$_{222}$- and UV$_{254}$-based AOPs. a,b, Logarithmic plots of the inactivation of MS2 bacteriophage spiked into authentic RO permeate samples from facilities 1–3 along with 100 μM (3.4 mg l^{-1}) H$_2$O$_2$ as a function of incident UV fluence for the UV$_{222}$-based AOP (**a**) and the UV$_{254}$-based AOP (**b**).

a higher quantum yield (Φ_{254} = 0.62 versus 0.50)[13], properties that promote radical production and radical-mediated degradation of chemical contaminants such as 1,4-dioxane[13–15]. Chlorine contact also contributes to pathogen inactivation. These factors suggest that AOP treatment goals could be attained at lower UV fluence, thereby reducing the energy intensity of AOP treatment. However, the reduction in UV fluence probably could not be realized because other research has demonstrated that chlorine reactions with inorganic chloramines in RO permeate lead to the formation of NDMA, necessitating an increase in UV fluence to control the additional NDMA[13,14,24].

Our results indicate that switching from 254 to 222 nm could be a more effective alternative than switching oxidants. After developing an accurate kinetic model for the UV$_{222}$-based AOP, we confirmed by both experiment and modelling that switching irradiation wavelength increased the steady-state concentration of radicals 3.6-fold in synthetic RO permeate (Table 2). Of the three treatment targets that potable reuse utilities must meet, 0.5-log removal of 1,4-dioxane was the most challenging across three RO permeate samples, necessitating on average ~320 mJ cm^{-2} incident UV fluence at 222 nm, a 4.1-fold reduction from the ~1,320 mJ cm^{-2} average needed at 254 nm. However, the strong absorbance by RO permeate constituents at 222 nm results in a shorter effective pathlength. Compensating for the reduced pathlength will require either decreasing the spacing between lamps and/ or increasing the lamp irradiance. As a result, the anticipated approximately fourfold reduction in energy may not be fully realized, with the extent of the effect dependent on the constitution and the resulting UV absorbance of a particular RO permeate. At 254 nm, NH$_2$Cl can be a dominant scavenger of UV photons (ε_{254} = 371 M^{-1} cm^{-1}; Table 1), but

it is difficult to avoid in RO permeate due to the common practice of applying inorganic chloramines upstream of RO membranes to control biofouling. The absorption by NH$_2$Cl is lower at 222 nm (Table 1), but nitrate becomes an important scavenger at this wavelength (ε_{222} = 2,747 M^{-1} cm^{-1})[23]. Thus, minimizing nitrate would maximize the effective pathlength at 222 nm. However, further research is needed on the net effect of nitrate at 222 nm because nitrate photolysis can generate HO·, which contributes to contaminant degradation (equation (8)), although the quantum yield for this reaction at 222 nm is not known. Nitrate photolysis also produces reactive nitrogen species (for example, O$_2$N·) that can react with organic matter to form DBPs (for example, chloropicrin)[35]. Despite these risks, switching to 222 nm increased the UV fluence-based degradation rate constants for halogenated DBPs up to approximately eightfold for DBPs with bromine substituents, which exhibit the highest cytotoxic potencies[36] and occur at concentrations close to levels of potential human health concern in RO permeate[31,32]. Further commercial development of lamps capable of efficient emission of 222 nm light is needed. While the efficiency of the mercury lamps currently used to deliver 254 nm light (~15–35%) exceeds that of excimer lamps delivering 222 nm light (5–15%), novel lamps based on cathodoluminescent field-emission chips are anticipated to surpass the efficiency of excimer lamps in the near future[37].

$$NO_3^- + H^+ + h\nu \rightarrow HO\cdot + O_2N\cdot \tag{7}$$
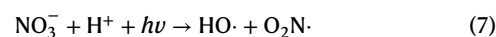
Methods
Reagents
The sources and purities of 1,4-dioxane, DBPs and probe compounds are provided in Supplementary Table 7. Stock solutions were prepared by diluting these reagents in deionized water. Stability tests confirmed that the degradation of these compounds in these stock solutions was negligible for over 2 weeks. Stock solutions of H$_2$O$_2$ and HOCl were prepared by diluting 30% H$_2$O$_2$ or ~6% sodium hypochlorite in deionized water and standardized spectrophotometrically (Agilent Cary 60 system) at 254 nm (ε_{254} = 18.6 M^{-1} cm^{-1}; Table 1) or 292 nm (ε_{292} = 365 M^{-1} cm^{-1})[38], respectively. The concentration of H$_2$O$_2$ was further verified by the I$_3^-$ method[39]. Stock solutions of NH$_2$Cl were prepared daily by titrating sodium hypochlorite into an ammonium chloride solution at a Cl/N molar ratio of 1:1.03 at pH 8.5. Stock solutions of NHCl$_2$ were prepared by adjusting the pH of the NH$_2$Cl solutions to 3.7 using phosphoric acid, equilibrating for 1 h and then refrigerating overnight with no headspace at 4 °C (ref. 12). The concentrations of NH$_2$Cl and NHCl$_2$ in the stock solutions were measured by N,N-diethyl-p-phenylenediamine (DPD)/ferrous ammonium sulfate (FAS) titration and cross-checked by measuring the UV absorbance at the absorption maxima of NH$_2$Cl (245 nm) and NHCl$_2$ (295 nm)[12].

The synthetic RO permeate was prepared by adding 70 μM sodium hypochlorite to 70 μM ammonium chloride in deionized water containing 0.5 mM sodium bicarbonate and 2 mM phosphate buffer. The solution was adjusted to pH 5.8 using H$_2$SO$_4$ and NaOH and kept in darkness with gentle mixing for 30 min before use. The NH$_2$Cl and NH$_2$Cl concentrations were measured as 35 μM (2.46 mg$_{Cl_2}$ l^{-1}) and 11 μM (1.62 mg$_{Cl_2}$ l^{-1}), respectively.

Grab samples of RO permeate were collected from three potable reuse facilities in California (facilities 1–3). The general water quality parameters are provided in Supplementary Table 3. Samples were maintained on ice with no headspace until experiments were initiated, and experiments were conducted within 24 h to minimize the evolution of chloramine species. The concentrations of NH$_2$Cl and NHCl$_2$ in the RO permeates were determined using the absorbances at 245 and 295 nm measured in a 10-cm quartz cuvette[12].

Preparation of virus
MS2 bacteriophage (DMS, no. 13767) was propagated in its host *Escherichia coli* (ATCC 700891) following EPA Method 1602 (ref. 40). Briefly, to

grow the *E. coli* host, 25 ml tryptic soy broth (pH 7.3 ± 0.2) containing the antibiotics ampicillin sodium salt and streptomycin sulfate (15 mg/L each) was inoculated with 20 µl *E. coli* stock and then incubated at 37 °C for ~3 h until the growth reached logarithmic phase.

Generation of the virus stock required high-titre lysed plates. These plates were made by inoculating 0.7% soft tryptic agar with 200 µl of the log-phase *E. coli* solution and 200 µl diluted stock virus (~10⁴ plaque-forming units per ml (PFU ml⁻¹)). The soft agar was then poured onto 1.5% hard tryptic soy agar plates and the plates were incubated upside down overnight at 37 °C. The following day, the soft agar from the completely lysed plates was scraped off the hard agar and combined with phosphate-buffered saline (PBS) solution (Fisher BioReagents) to elute the virus into PBS solution. To remove bacteria, large cell fragments and remaining agar from the solution, we centrifuged the mixture and filtered the supernatant through a 0.45-µm pore-sized filter followed by a 0.22-µm pore-sized filter. To remove nutrients and colour left from the culturing process from the virus stock, the filtrate was washed three times with PBS in an Amicon Ultra-15 centrifugal filter unit (EMD Millipore). The Amicon Ultra-15 centrifugal filter unit had a 100,000 Da molecular weight cut-off, which, unlike the pore filters used earlier, was able to retain viruses and allow concentration and purification of the virus stock. The virus concentrate (0.85 ml) obtained from the Amicon Ultra-15 centrifugal filter unit after washing was combined with 0.15 ml autoclaved glycerol and stored at −80 °C until use in experiments.

To characterize the purity of our viral stock solution, we measured the UV absorbance (200–300 nm) of the viral stock solution (virus + matrix) and compared it with the absorbance of the viral stock matrix alone (Extended Data Fig. 9). The stock matrix was created in the same way as the viral stock, but without the addition of any virus. Briefly, bacteria were added to soft agar, poured onto hard agar plates and incubated. After incubation, the soft agar was combined with PBS, filtered and washed in the same manner as described previously. The absorbance values for deionized water and RO permeates from the three potable reuse facilities are provided in Extended Data Fig. 9. At 225 nm, the difference in the absorbance of deionized water and the viral stock was 0.13 cm⁻¹, while the difference in the absorbance of deionized water and the viral stock matrix was 0.05 cm⁻¹. These were the largest absorbance differences observed between 222 and 254 nm for these solutions. These differences suggest that the absorbance arose predominantly from the virus rather than the matrix, and therefore that the viral stock solution was sufficiently pure so as not to interfere with UV inactivation.

UV set-up

The UV irradiation was provided by either a low-pressure (LP) mercury lamp (Philips, TUV 15W/G15T8) emitting UV radiation at 254 nm or a KrCl* excimer lamp (Ergo HealthTech, Ltd., 15W/A65) emitting UV radiation at 222 nm. The excimer lamp was equipped with a band-gap filter to filter out emission >230 nm. The emission spectra of the LP UV and excimer lamps were recorded using a spectroradiometer (International Light Technologies, ILT960UVLS-RAA4) and are shown in Extended Data Fig. 10. The UV light from the lamps was directed down onto the water samples in cylindrical crystallization dishes (4.4 cm diameter × 4.5 cm depth; the exterior of the dishes was wrapped in black duct tape) with rapid mixing by magnetic stir bars. The reactors were covered with quartz plates to prevent the evaporation of chemicals during UV irradiation. The incident fluence rates from the reactors were measured by KI–KIO₃ actinometry[28] as 0.53 ± 0.05 mW cm⁻² for 254 nm light and 1.10 ± 0.03 mW cm⁻² for 222 nm light.

Experimental procedures

Experiments were conducted to compare the degradation rate constants for the halogenated DBPs, *N*-nitrosamines and 1,4-dioxane by direct UV photolysis and the UV/H₂O₂ AOP (in the presence and absence of chloramines) in deionized water and authentic RO permeate samples collected from three potable reuse facilities. The degradation rate constants by direct photolysis at 222 and 254 nm were measured separately for each contaminant by irradiating 1 µM of each contaminant in deionized water and collecting samples to analyse the remaining concentration of contaminant. First-order degradation rate constants (k_{obs}) were obtained from the slopes of plots of ln (C/C_o) versus time. Similar procedures were followed in the presence of 100 µM H₂O₂ in synthetic RO permeate with and without chloramines. For experiments conducted using authentic RO permeates, low levels of halogenated DBPs were measured in the samples. The samples were spiked with 100 µg l⁻¹ halogenated DBPs, 50 ng l⁻¹ NDMA or 1 µM 1,4-dioxane to facilitate measurement of the remaining contaminant concentrations over time.

For experiments with MS2 bacteriophage, three aliquots of 50 ml of the RO permeate samples were each spiked with 500 µl MS2 stock (~1,010 PFU ml⁻¹) at room temperature, yielding a 1:100 dilution of the viral stock. Each RO permeate sample was then subjected to three conditions: (1) darkness (no UV application), (2) irradiation at 222 nm and (3) irradiation at 254 nm. Five 1 ml samples from the RO permeate solutions under UV conditions were withdrawn over time, and three 1 ml samples under the dark condition were removed over time. The samples were stored on ice in the dark until quantification within a maximum of 3 h after sample collection.

Measurement of steady-state concentrations of radicals

Nitrobenzene (NB) and benzoic acid (BA) were used as probes to measure the steady-state concentrations of HO· and Cl· formed from the photolysis of H₂O₂ and chloramines. These probes have been used to measure steady-state radical concentrations in many complicated systems, including UV/chlorine, UV/persulfate and UV/chloramine AOP systems[29,34,41]. NB is highly reactive with HO· ($k = 3.9 \times 10^9\,M^{-1}\,s^{-1}$)[28], but not with Cl· or Cl₂·⁻ (ref. 28), such that the observed first-order degradation rate constant probes HO· reactions (equation (8)). Here $k_{obs,NB}$ is the observed first-order degradation rate constant of NB, and $k_{HO·-NB}$ is the second-order reaction rate constant between NB and HO·. BA is reactive with both HO· ($k = 5.5 \times 10^9\,M^{-1}\,s^{-1}$) and Cl· ($k = 1.8 \times 10^{10}\,M^{-1}\,s^{-1}$)[42], but not with Cl₂·⁻ (ref. 42), such that the first-order degradation rate constant of BA enables calculation of the steady-state concentration of Cl· (equation (9)). Here $k_{obs,BA}$ is the observed first-order degradation rate constant of BA, and $k_{HO·-BA}$ and $k_{Cl·-BA}$ are the second-order reaction rate constants between BA and HO· and Cl·, respectively.

$$k_{obs,NB} = k_{HO·-NB}[HO·]_{ss} \tag{8}$$

$$k_{obs,BA} = k_{HO·-BA}[HO·]_{ss} + k_{Cl·-BA}[Cl·]_{ss} \tag{9}$$

Analytical methods

The NB and BA probe concentrations were measured by high-performance liquid chromatography (Agilent, Infinity 1260 system) using a UV–visible detector and an Agilent C18 column[34]. The concentrations of halogenated DBPs were measured by gas chromatography (Agilent, 6890N system) using a micro-electron capture detector following methods described previously[30]. The concentrations of NDMA and NMOR were measured by gas chromatography tandem mass spectrometry with methanol chemical ionization (Agilent, 7890N gas chromatograph coupled to a 240 ion trap mass spectrometer) following EPA Method 521 modified as described previously[32].

MS2 bacteriophage was quantified using a double-layer plaque assay procedure based on EPA Method 1602. Briefly, 200 µl log-phase *E. coli* and 200 µl diluted sample were added to 0.7% soft tryptic soy agar and then poured onto 1.5% hard tryptic soy agar plates. The plates were incubated upside down overnight at 37 °C and then PFUs were

recorded. Countable PFUs were in the range 1–300 PFU. Samples in which all plated dilutions were above the limit of detection (that is, >300 PFU) were assayed again the following day (after storage at 4 °C in the dark) at higher dilutions. Negative and positive controls were included in each experiment. Negative controls involved plating with *E. coli* and PBS; positive controls were plated with *E. coli* and the diluted viral stock. The log reduction of virus was calculated using equation (10):

$$\text{log reduction} = -\log_{10}\left(\frac{N}{N_0}\right) \quad (10)$$

where N is the average PFU × dilution factor for the six plates (three dilutions plated in duplicate) at each time point and N_0 is the average PFU × dilution factor for the plates at time zero. Samples below the limit of detection (1 PFU) or above the limit of detection (300 PFU) were not used in the average PFU × dilution factor calculation. If the undiluted sample plate was below the limit of detection, the log reduction could not be determined.

Kinetic modelling and determination of quantum yields

A kinetic model of the UV/H_2O_2 AOP was implemented using Kintecus software (version 4.55; http://www.kintecus.com/) to determine the innate quantum yields for the UV photolysis of H_2O_2, NH_2Cl and $NHCl_2$ to predict the steady-state concentrations of radicals and compare the experimental and modelled degradation of contaminants. The 119 elementary steps contained within the model are provided in Supplementary Table 4. The model was examined in terms of detailed balancing using the DETBAL software[43].

To measure the photodecay quantum yields at 222 nm, pseudo-first-order photodecay rate constants (k_{obs}) for H_2O_2, NH_2Cl and $NHCl_2$ were determined in separate experiments for each oxidant by measuring the time-dependent change in oxidant concentrations under 222 nm radiation at pH 7.0. The Φ value for each oxidant was fitted by assigning different values to Φ within the kinetic model and comparing the modelled time-dependent photodecay rate constants ($k_{modelled}$) with the experimentally determined rate constants (k_{obs}). The error (square of errors) is defined as the square of the difference between the two rate constants, that is, $(k_{modelled} - k_{obs})^2$ (ref. 12). The optimal Φ values were those that minimized this error (Extended Data Fig. 4).

Statistical analysis

All tests were conducted in duplicate. The data were plotted as the mean of the duplicated experiments. For MS2 bacteriophage analyses, the individual data points provided in Fig. 3 represent the average PFUs from plates featuring 1–300 PFUs obtained from duplicate experiments at three different dilutions (that is, up to six plates). Statistical significance ($P < 0.05$) was evaluated by one-way analysis of variance (ANOVA; two-sided) using Origin 8.0 software (https://www.originlab.com/origin). When comparing the degradation of chemical contaminants, the first-order degradation rate constants were determined by regression analysis using the slopes of plots of ln (C/C_o) versus UV fluence. The average relative percentage difference between the slopes obtained from the duplicate experiments was <10%. The slopes for each of the duplicate experiments using the three RO permeate samples irradiated at 222 and 254 nm were then compared by the ANOVA test ($N = 6$). For experiments involving the inactivation of MS2 bacteriophage, the slopes of plots of log (N/N_o) versus UV fluence for each of the duplicate experiments in the three RO permeate samples irradiated at 222 and 254 nm were compared by the ANOVA test ($N = 6$).

Data availability

Source data are provided with this paper. The Extended Data figures contain the datasets analysed to develop Figs. 1 and 2 in the main text.

References

1. McDonald, R. I. et al. Urban growth, climate change, and freshwater availability. *Proc. Natl Acad. Sci. USA* **108**, 6312–6317 (2011).
2. Hoekstra, A. Y. Water scarcity challenges to business. *Nat. Clim. Change* **4**, 318–320 (2014).
3. He, C. et al. Future global urban water scarcity and potential solutions. *Nat. Commun.* **12**, 4667 (2021).
4. Giammar, D. E. et al. Cost and energy metrics for municipal water reuse. *ACS ES T Eng.* **2**, 489–507 (2022).
5. Keller, A. A., Su, Y. & Jassby, D. Direct potable reuse: are we ready? A review of technological, economic, and environmental considerations. *ACS ES T Eng.* **2**, 273–291 (2022).
6. Rodriguez, C. et al. Indirect potable reuse: a sustainable water supply alternative. *Int. J. Environ. Res. Public Health* **6**, 1174–1209 (2009).
7. Stanford, B. D. et al. Planning for direct potable reuse: operational aspects of an integrated drinking water system. *J. Am. Water Works Assoc.* **108**, 48–55 (2016).
8. Gerrity, D., Pecson, B., Trussell, R. S. & Trussell, R. R. Potable reuse treatment trains throughout the world. *Aqua* **62**, 321–338 (2013).
9. Marron, E. L., Mitch, W. A., von Gunten, U. & Sedlak, D. L. A tale of two treatments: the multiple barrier approach to removing chemical contaminants during potable water reuse. *Acc. Chem. Res.* **52**, 615–622 (2019).
10. Sim, A. & Mauter, M. S. Cost and energy intensity of US potable water reuse systems. *Environ. Sci. Water Res. Technol.* **7**, 748–761 (2021).
11. Pype, M. L., Lawrence, M. G., Keller, J. & Gernjak, W. Reverse osmosis integrity monitoring in water reuse: the challenge to verify virus removal—a review. *Water Res.* **98**, 384–395 (2016).
12. Zhang, Z., Chuang, Y. H., Huang, N. & Mitch, W. A. Predicting the contribution of chloramines to contaminant decay during ultraviolet/hydrogen peroxide advanced oxidation process treatment for potable reuse. *Environ. Sci. Technol.* **53**, 4416–4425 (2019).
13. Chuang, Y.-H. et al. Pilot-scale comparison of microfiltration/reverse osmosis and ozone/biological activated carbon with UV/hydrogen peroxide or UV/free chlorine AOP treatment for controlling disinfection byproducts during wastewater reuse. *Water Res.* **152**, 215–225 (2019).
14. Szczuka, A. et al. *N*-Nitrosodimethylamine formation during UV/hydrogen peroxide and UV/chlorine advanced oxidation process treatment following reverse osmosis for potable reuse. *Environ. Sci. Technol.* **54**, 15465–15475 (2020).
15. Chuang, Y. H., Chen, S., Chinn, C. J. & Mitch, W. A. Comparing the UV/monochloramine and UV/free chlorine advanced oxidation processes (AOPs) to the UV/hydrogen peroxide AOP under scenarios relevant to potable reuse. *Environ. Sci. Technol.* **51**, 13859–13868 (2017).
16. Blatchley, E. R. et al. Far UV-C radiation: an emerging tool for pandemic control. *Crit. Rev. Environ. Sci. Technol.* **53**, 733–753 (2022).
17. Welch, D. et al. Far-UVC light: a new tool to control the spread of airborne-mediated microbial diseases. *Sci. Rep.* **8**, 2758 (2018).
18. Türsen, Ü., Türsen, B. & Lotti, T. Ultraviolet and COVID-19 pandemic. *J. Cosmet. Dermatol.* **19**, 2162–2164 (2020).
19. Barnard, I. R. M., Eadie, E. & Wood, K. Further evidence that far-UVC for disinfection is unlikely to cause erythema or pre-mutagenic DNA lesions in skin. *Photodermatol. Photoimmunol. Photomed.* **36**, 476–477 (2020).
20. Ma, B., Gundy, P. M., Gerba, C. P., Sobsey, M. D. & Linden, K. G. UV inactivation of SARS-CoV-2 across the UVC spectrum: KrCl* excimer, mercury-vapor, and light-emitting-diode (LED) sources. *Appl. Environ. Microbiol.* **87**, e01532-21 (2021).

21. Ma, B. et al. Inactivation of coronaviruses and phage Phi6 from irradiation across UVC wavelengths. *Environ. Sci. Technol. Lett.* **8**, 425–430 (2021).

22. Ma, B. et al. Inactivation of biofilm-bound bacterial cells using irradiation across UVC wavelengths. *Water Res.* **217**, 118379 (2022).

23. Payne, E. M., Liu, B., Mullen, L. & Linden, K. G. UV 222 nm emission from KrCl* excimer lamps greatly improves advanced oxidation performance in water treatment. *Environ. Sci. Technol. Lett.* **9**, 779–785 (2022).

24. McCurry, D. L., Ishida, K. P., Oelker, G. L. & Mitch, W. A. Reverse osmosis shifts chloramine speciation causing re-formation of NDMA during potable reuse of wastewater. *Environ. Sci. Technol.* **51**, 8589–8596 (2017).

25. Rosenfeldt, E. J. & Linden, K. G. Degradation of endocrine disrupting chemicals bisphenol A, ethinyl estradiol, and estradiol during UV photolysis and advanced oxidation processes. *Environ. Sci. Technol.* **38**, 5476–5483 (2004).

26. Bolton, J. R., Mayor-Smith, I. & Linden, K. G. Rethinking the concepts of fluence (UV dose) and fluence rate: the importance of photon-based units—a systemic review. *Photochem. Photobiol.* **91**, 1252–1262 (2015).

27. Bolton, J. R., Stefan, M. I., Shaw, P. S. & Lykke, K. R. Determination of the quantum yields of the potassium ferrioxalate and potassium iodide–iodate actinometers and a method for the calibration of radiometer detectors. *J. Photochem. Photobiol. A* **222**, 166–169 (2011).

28. Bulman, D. M., Mezyk, S. P. & Remucal, C. K. The impact of pH and irradiation wavelength on the production of reactive oxidants during chlorine photolysis. *Environ. Sci. Technol.* **53**, 4450–4459 (2019).

29. Guo, K., Wu, Z., Chen, C. & Fang, J. UV/chlorine process: an efficient advanced oxidation process with multiple radicals and functions in water treatment. *Acc. Chem. Res.* **55**, 286–297 (2022).

30. Chuang, Y.-H., Parker, K. M. & Mitch, W. A. Development of predictive models for the degradation of halogenated disinfection byproducts during the UV/H₂O₂ advanced oxidation process. *Environ. Sci. Technol.* **50**, 11209–11217 (2016).

31. Lau, S. S. et al. Toxicological assessment of potable reuse and conventional drinking waters. *Nat. Sustain.* **6**, 39–46 (2023).

32. Lau, S. S., Forster, A. L., Richardson, S. D. & Mitch, W. A. Disinfection byproduct recovery during extraction and concentration in preparation for chemical analyses or toxicity assays. *Environ. Sci. Technol.* **55**, 14136–14145 (2021).

33. Plumlee, M. H., Stanford, B. D., Debroux, J.-F., Hopkins, D. C. & Snyder, S. A. Costs of advanced treatment in water reclamation. *Ozone Sci. Eng.* **36**, 485–495 (2014).

34. Yin, R., Blatchley, E. R. & Shang, C. UV photolysis of mono- and dichloramine using UV-LEDs as radiation sources: photodecay rates and radical concentrations. *Environ. Sci. Technol.* **54**, 8420–8429 (2020).

35. Shah, A. D., Dotson, A. D., Linden, K. G. & Mitch, W. A. Impact of UV disinfection combined with chlorination/chloramination on the formation of halonitromethanes and haloacetonitriles in drinking water. *Environ. Sci. Technol.* **45**, 3657–3664 (2011).

36. Wagner, E. D. & Plewa, M. J. CHO cell cytotoxicity and genotoxicity analyses of disinfection by-products: an updated review. *J. Environ. Sci.* **58**, 64–76 (2017).

37. Sharma, V. K. & Demir, H. V. Bright future of deep-ultraviolet photonics: emerging UVC chip-scale light-source technology platforms, benchmarking, challenges, and outlook for UV disinfection. *ACS Photonics* **9**, 1513–1521 (2022).

38. Feng, Y., Smith, D. W. & Bolton, J. R. Photolysis of aqueous free chlorine species (HOCl and OCl) with 254 nm ultraviolet light. *J. Environ. Eng. Sci.* **6**, 277–284 (2007).

39. Klassen, N. V., Marchington, D. & McGowan, H. C. E. H₂O₂ determination by the I₃⁻ method and by KMnO₄ titration. *Anal. Chem.* **66**, 2921–2925 (1994).

40. *Method 1602: Male-Specific (F⁺) and Somatic Coliphage in Water by Single Agar Layer (SAL) Procedure* EPA 821-R-01-029 (USEPA, 2001).

41. Li, W. et al. UV photolysis of chloramine and persulfate for 1,4-dioxane removal in reverse-osmosis permeate for potable water reuse. *Environ. Sci. Technol.* **52**, 6417–6425 (2018).

42. Fang, J., Fu, Y. & Shang, C. The roles of reactive species in micropollutant degradation in the UV/free chlorine system. *Environ. Sci. Technol.* **48**, 1859–1868 (2014).

43. Stanbury, D. M. Mechanisms of advanced oxidation processes, the principle of detailed balancing, and specifics of the UV/chloramine process. *Environ. Sci. Technol.* **54**, 4658–4663 (2020).

Author contributions

R.Y. and W.A.M. designed the project. R.Y., C.E.A. and J.Z. conducted the experiments. A.B.B. oversaw the pathogen inactivation experiments. R.Y. and W.A.M. wrote the paper.

Competing interests

The authors declare no competing interests.

Additional information

Extended data is available for this paper at https://doi.org/10.1038/s44221-023-00094-5.

Supplementary information The online version contains supplementary material available at https://doi.org/10.1038/s44221-023-00094-5.

Correspondence and requests for materials should be addressed to William A. Mitch.
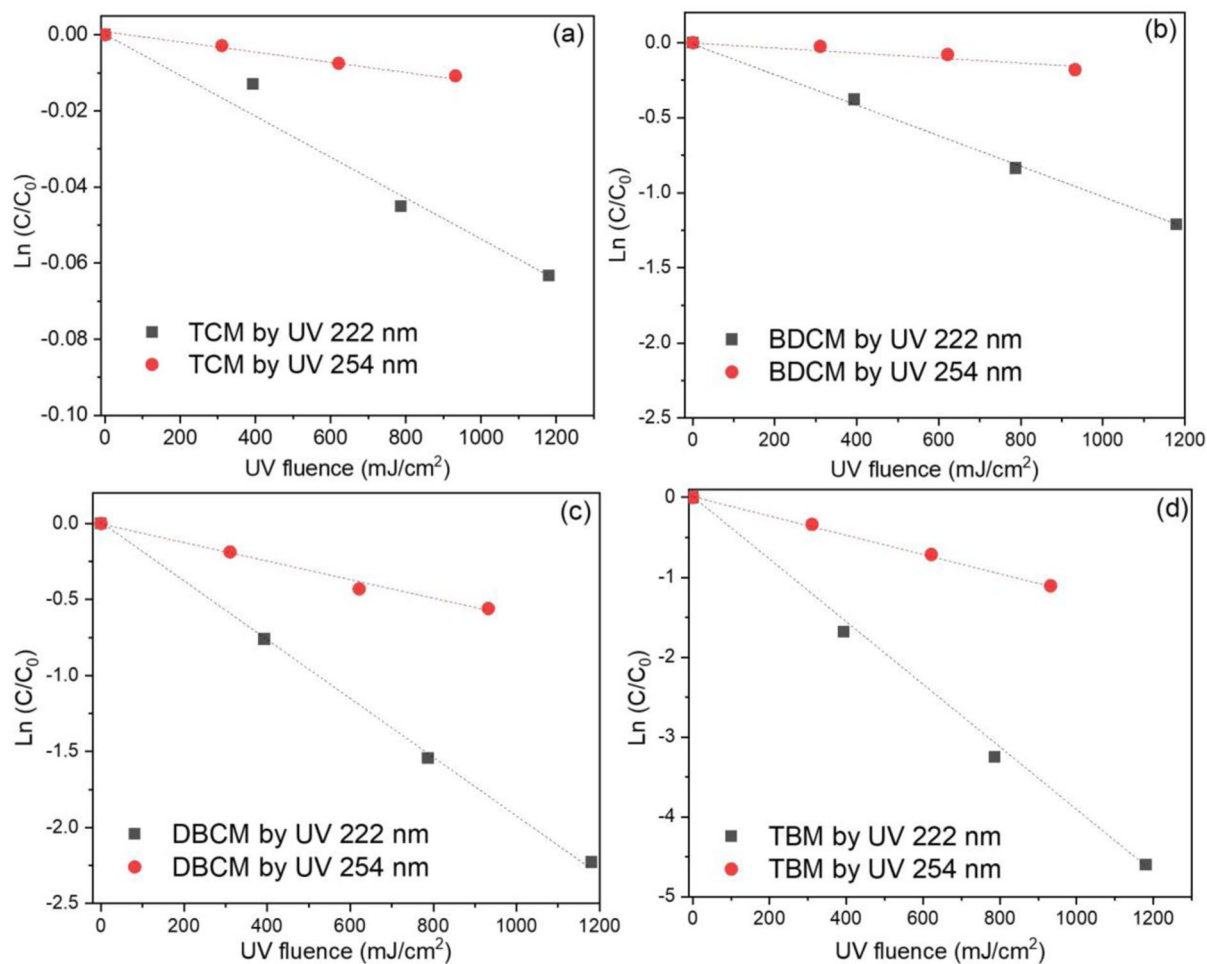
Peer review information *Nature Water* thanks the anonymous reviewers for their contribution to the peer review of this work.

Reprints and permissions information is available at www.nature.com/reprints.
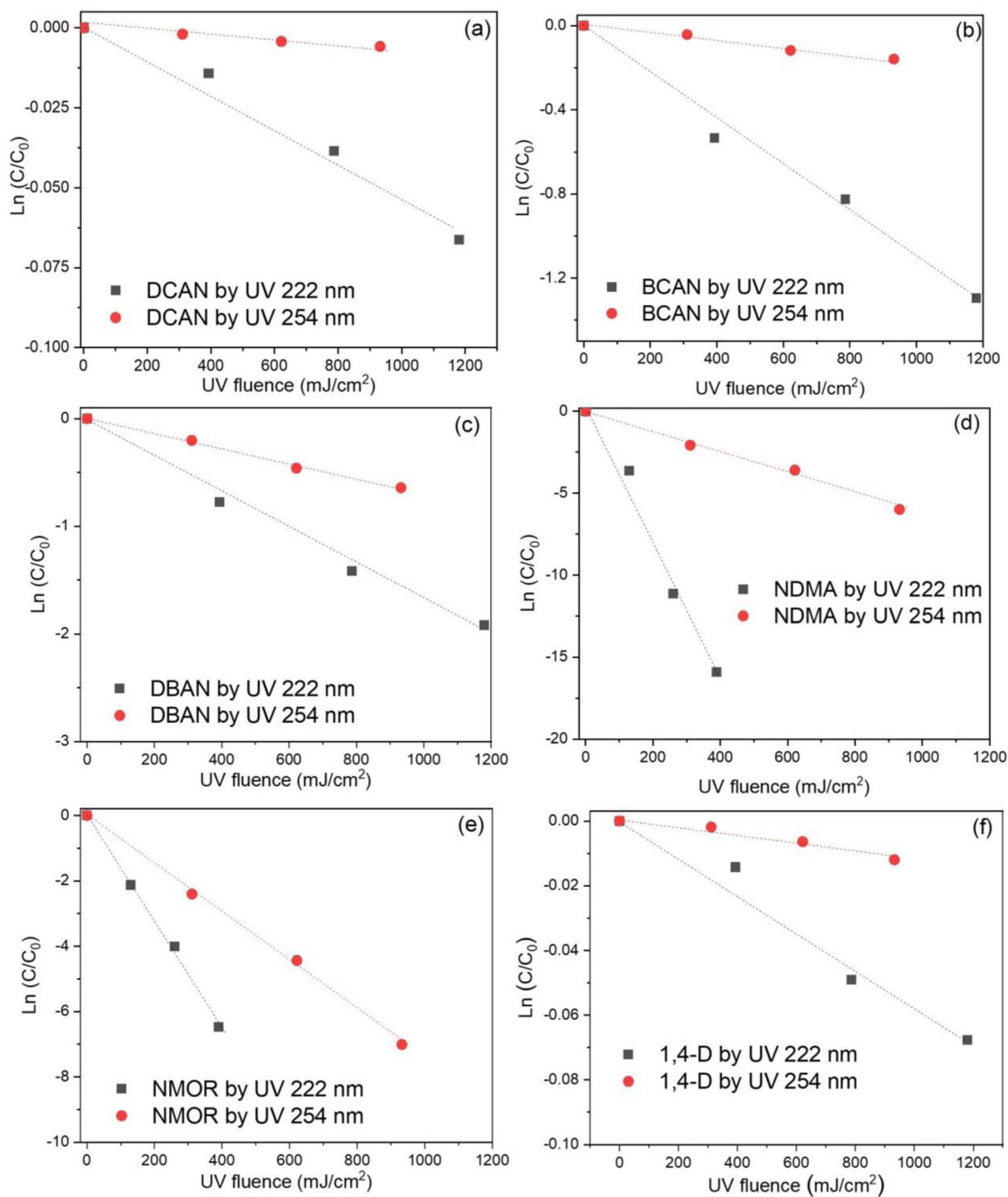
Publisher's note Springer Nature remains neutral with regard to jurisdictional claims in published maps and institutional affiliations.

Extended Data Fig. 1 | Direct photolysis of trihalomethanes. Degradation of four trihalomethanes (THMs) (**a** – **d**) by direct UV photolysis at 222 nm and 254 nm in deionized water.

Extended Data Fig. 2 | Direct photolysis of compounds. Degradation of three haloacetonitriles (HANs) (**a** – **c**), two *N*-nitrosamines (**d** and **e**), and 1,4-dioxane (**f**) by direct UV photolysis at 222 nm and 254 nm in deionized water.
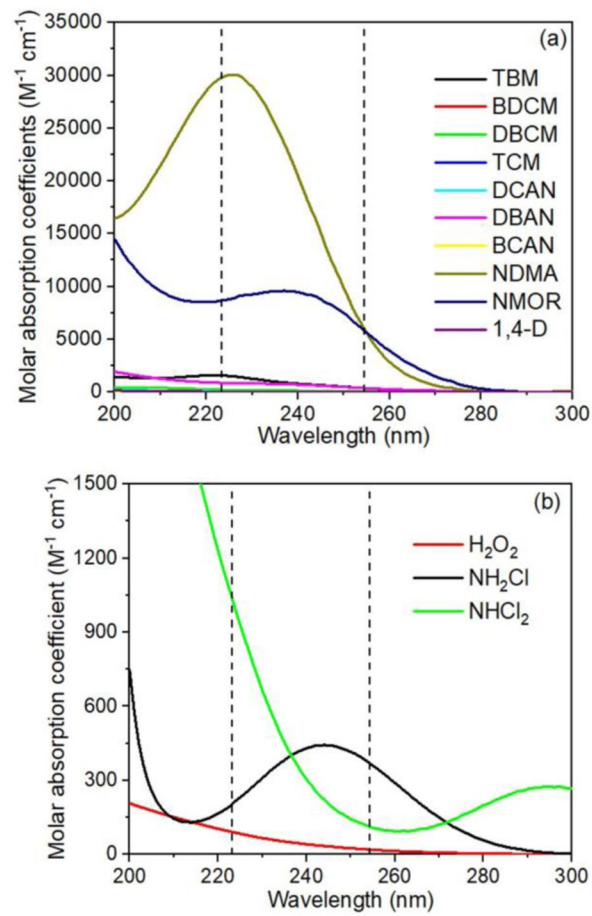
Extended Data Fig. 3 | Absorption spectra. The absorption spectra of contaminants (**a**) and oxidants (**b**) tested in this study.
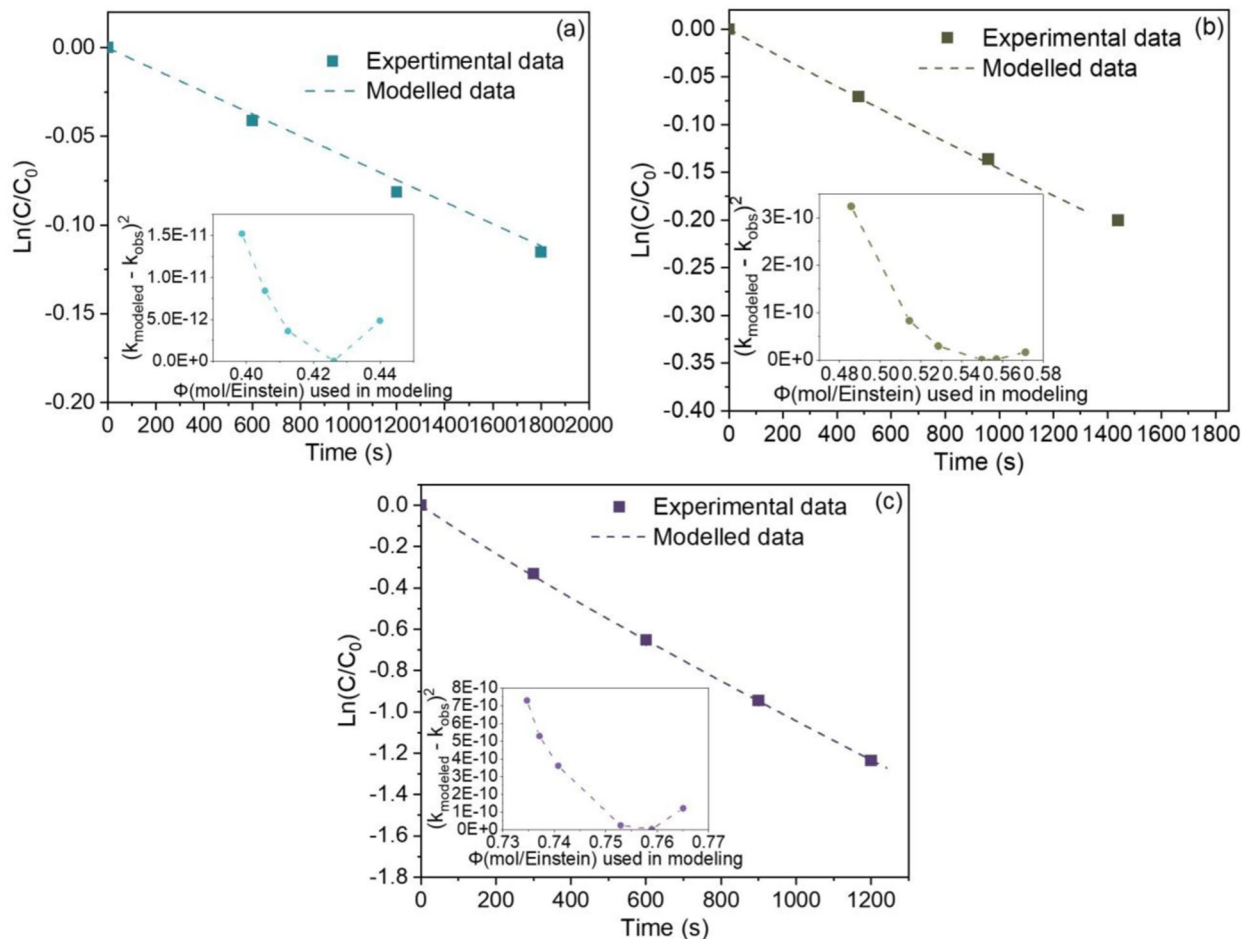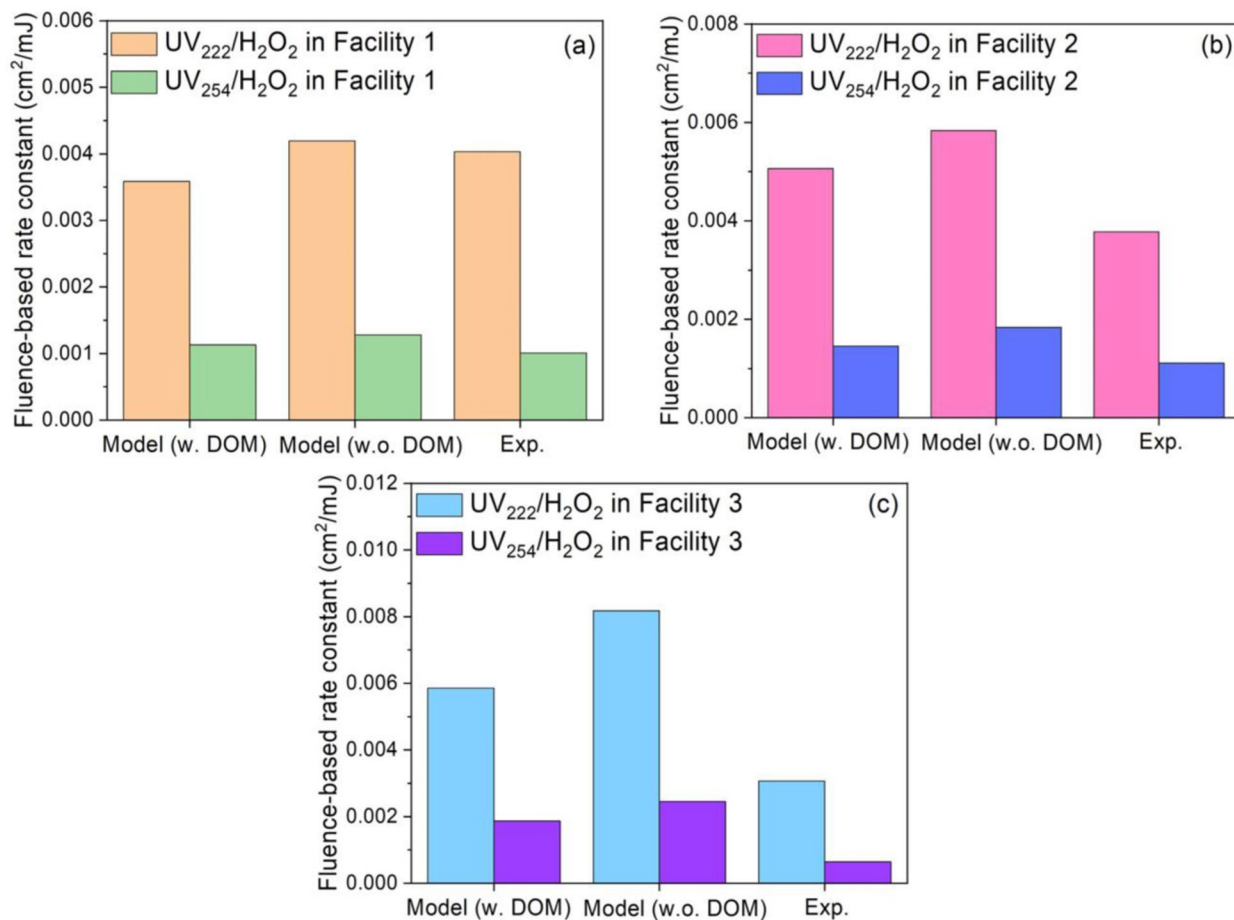
Extended Data Fig. 4 | Experimental vs. modelled losses of oxidants. Loss of (**a**) H_2O_2; (**b**) NH_2Cl; (**c**) $NHCl_2$ under UV_{222} photolysis. $[H_2O_2]_0 = [NH_2Cl]_0 = [NHCl_2]_0 = 70.4\ \mu M$, and $pH = 7.0$.
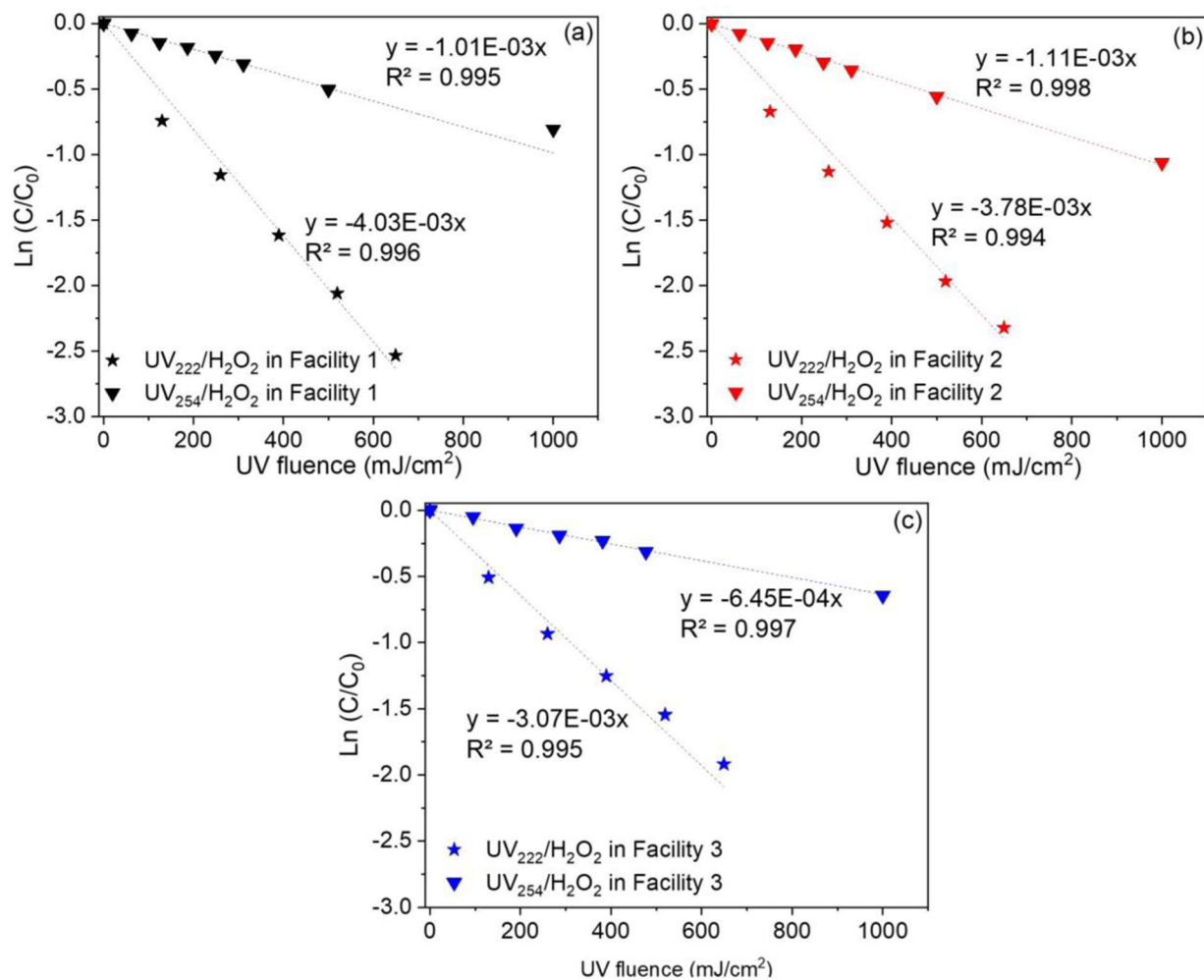
Extended Data Fig. 5 | The fluence-based degradation kinetics of 1,4-dioxane in the three RO permeates by the two UV-AOPs. Figures (**a**), (**b**), and (**c**) refer to Facilities 1, 2, and 3, respectively. Conditions: $[H_2O_2]_0 = 100\,\mu M$, $[1,4\text{-dioxane}]_0 = 1\,\mu M$.
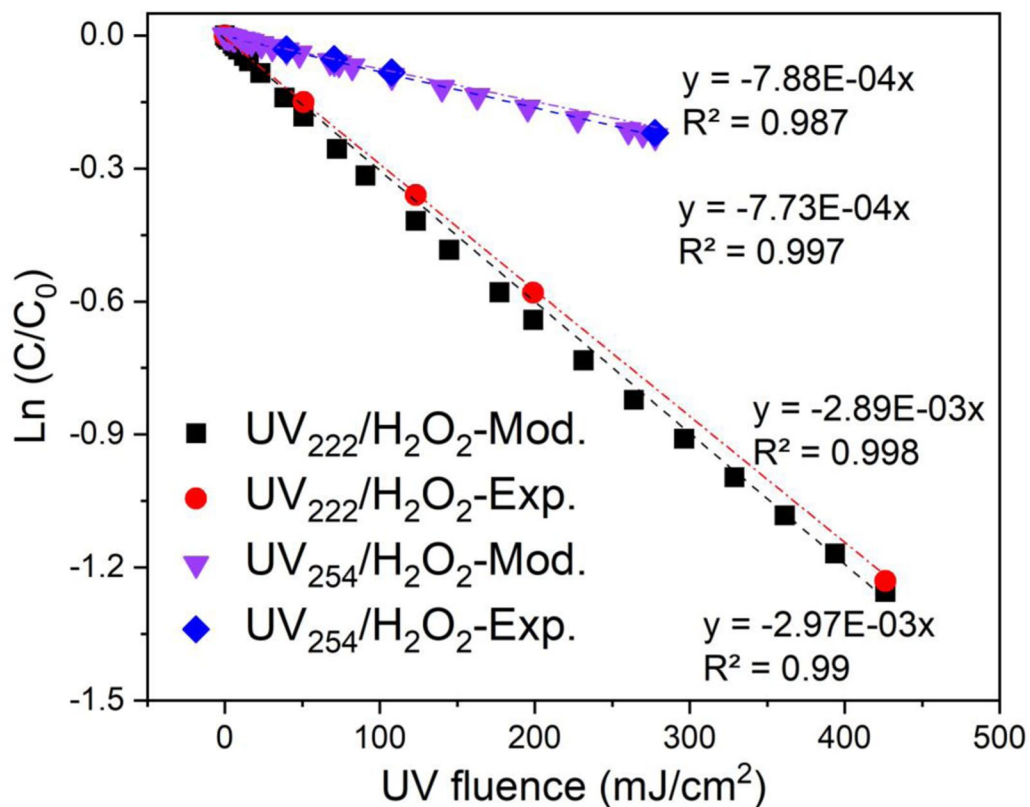
Extended Data Fig. 6 | Comparison between the model-predicted and experimental data for 1,4-dioxane degradation in synthetic RO permeate. Conditions: $[H_2O_2]_0 = 100\,\mu M$, $[1,4\text{-dioxane}]_0 = 1\,\mu M$, $[NH_2Cl]_0 = 3.5\,mg\text{-}Cl_2/L$, $[NHCl_2]_0 = 1.5\,mg\text{-}Cl_2/L$, $[HCO_3^-]_0 = 50\,mg/l$, pH = 5.6, and UV fluence rate = 1.1 mW/cm^2.

Extended Data Fig. 7 | Comparison between the modeled (that is, with or without considering the presence of dissolved organic matter (DOM)) and experimental results for the fluence-based degradation rate constants of 1,4-dioxane in authentic RO permeates from potable reuse facilities. Figures (a), (b), and (c) refer to Facilities 1, 2, and 3, respectively. Conditions: $[H_2O_2]_0 = 100 \ \mu M$, $[1,4\text{-dioxane}]_0 = 1 \ \mu M$. Chloramine concentrations and other water quality parameters correspond to Supplementary Table 3. For modeling DOM, the modeling assumed $[TOC]_0 = 0.25$ mg-C/L and $k_{OH\text{-}DOM} = 2.1 \times 10^4$ $(mg/l)^{-1}$ s^{-1})[19]. The incorporation of reactions with DOM improved the accuracy of the model. However, since DOM represents a diverse array of constituents, research is needed to better characterize and constrain the reactivity of DOM in RO permeate.
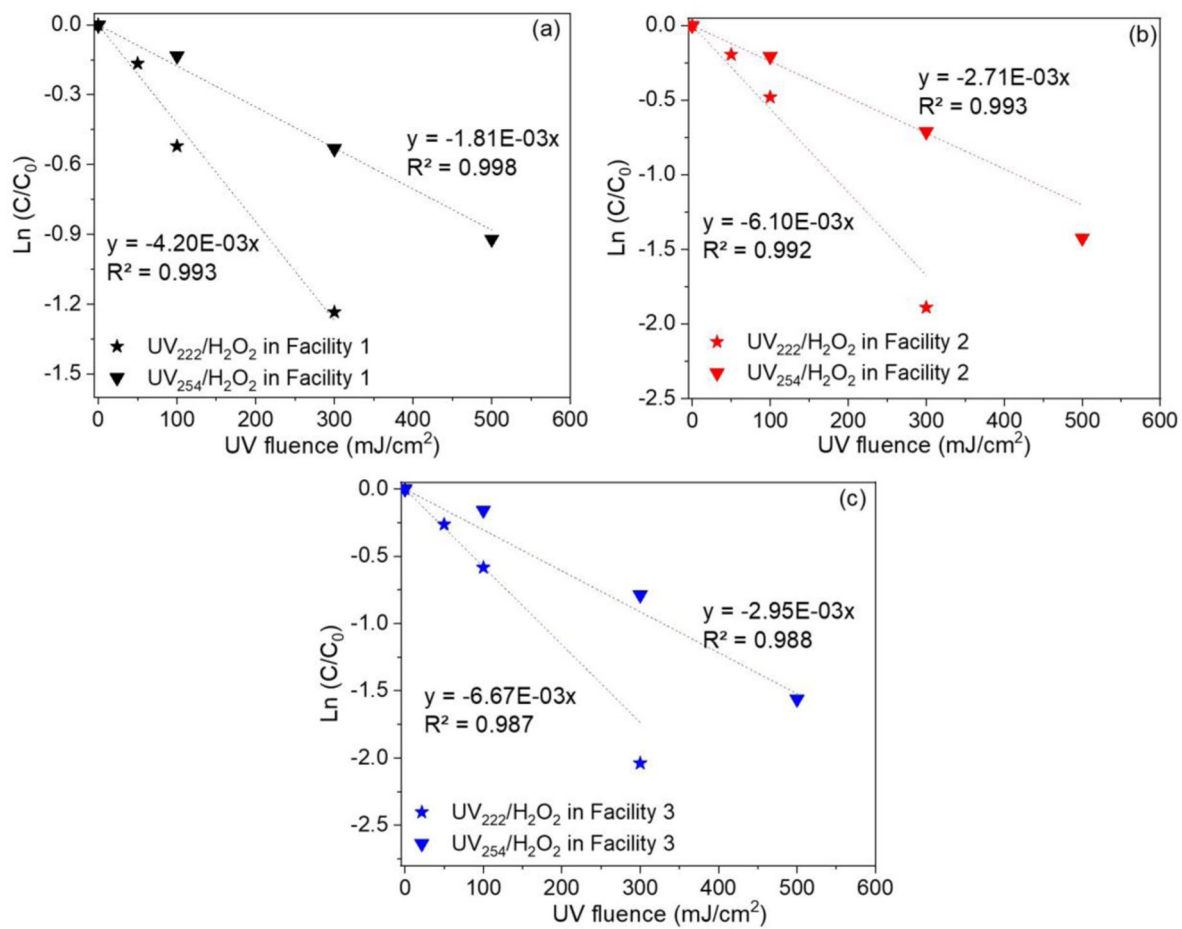
Extended Data Fig. 8 | The fluence-based degradation kinetics of NDMA by the two UV-AOPs in the RO permeates. Results are from Facilities **a)** 1, **b)** 2, and **c)** 3, respectively. Conditions: $[H_2O_2]_0 = 100 \, \mu M$, $[NDMA]_0 = 50 \, ng/l$.
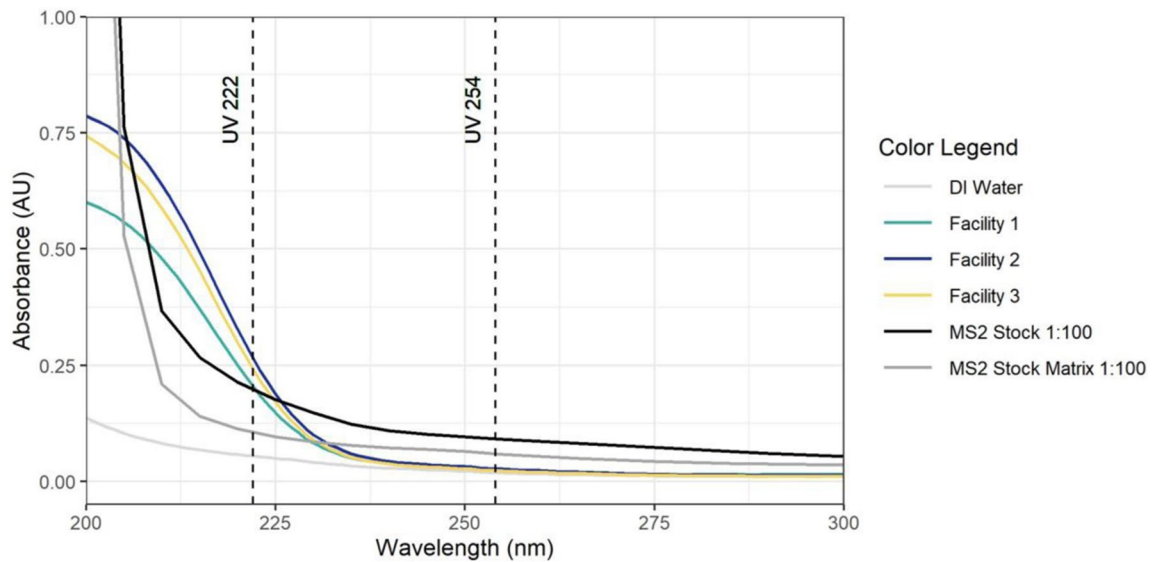
Extended Data Fig. 9 | RO permeate absorbance is shown for 200 to 300 nm for each RO permeate tested, MS2 stock (which contains both the virus and stock matrix), and MS2 stock matrix (which does not contain any virus). MS2 stock and MS2 stock matrix were diluted 1:100 in PBS. In experiments MS2 stock was diluted 1:100 in RO permeate. DI water absorbance is also plotted for comparison.
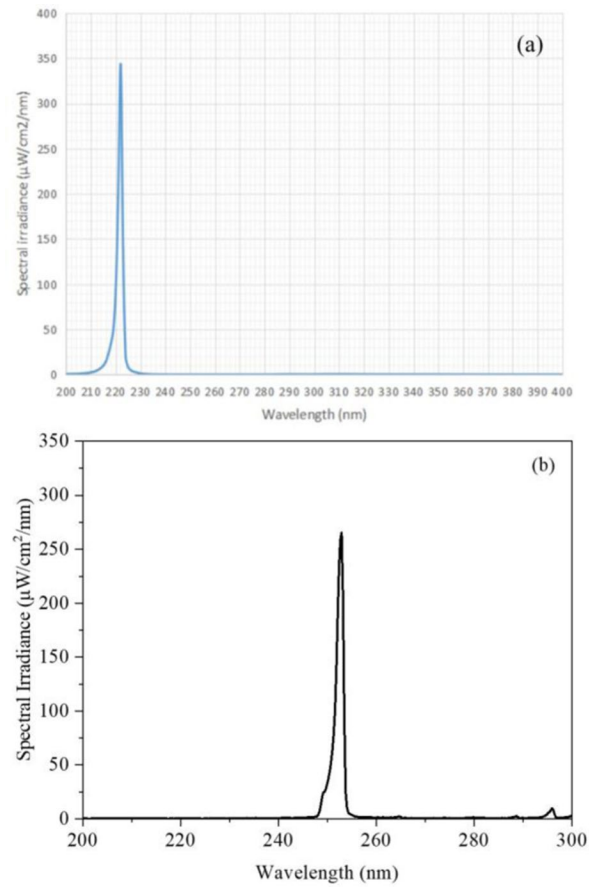
Extended Data Fig. 10 | Lamp emission spectra. The emission spectra of (**a**) the KrCl* excimer lamp and (**b**) the low-pressure mercury UV lamp.